GEOPHYSICS, VOL. 75, NO. 2 (MARCH-APRIL 2010); P. E101–E114, 12 FIGS., 3 TABLES.
10.1190/1.3336959

Simulation of full responses of a triaxial induction tool in a homogeneous biaxial anisotropic formation

Ning Yuan[1], Xiao Chun Nie[1], Richard Liu[1], and Cheng Wei Qiu[2]

ABSTRACT

Triaxial induction tools are used to evaluate fractured and low-resistivity reservoirs composed of thinly laminated sand-shale sequences. Thinly laminated and fractured reservoirs demonstrate transversely isotropic or fully anisotropic (biaxial anisotropic) electrical properties. Compared to the number of studies on transverse isotropy, relatively little work covers biaxial anisotropy because of the mathematical complexity. We have developed a theoretical analysis for the full response of a triaxial induction tool in a homogeneous biaxial anisotropic formation. The triaxial tool is composed of three mutually orthogonal transmitters and three mutually orthogonal receivers. The bucking coils are also oriented at three mutually orthogonal directions to remove direct coupling. Starting from the space-domain Maxwell's equations, which the electromagnetic (EM) fields satisfied, we obtain the spectral-domain Maxwell's equations by defining a Fourier transform pair. Solving the resultant spectral-domain vector equation, we can find the spectral-domain solution for the electric field. Then, the magnetic fields can be determined from a homogeneous form of Maxwell's equations. The solution for the EM fields in the space domain can be expressed in terms of inverse Fourier transforms of their spectral-domain counterparts. We use modified Gauss-Laguerre quadrature and contour integration methods to evaluate the inverse Fourier transform efficiently. Our formulations are based on arbitrary relative dipping and azimuthal and tool angles; thus, we obtain the full coupling matrix connecting source excitations to magnetic field response. We have validated our formulas and investigated the effects of logging responses on factors such as relative dipping, azimuthal and tool angles, and frequency using our code. We only consider conductivity anisotropy, not anisotropy in dielectric permittivity and magnetic permeability. However, our method and formulas are straightforward enough to consider anisotropy in dielectric permittivity.

INTRODUCTION

Electrical conductivity/resistivity logs provide valuable information about the porosity and fluid content of rock near a borehole. Conventional electric logs determine apparent scalar (or isotropic) conductivity. The conductivity is actually a symmetric and positive definite second-rank tensor (Kunz and Moran, 1958). In the principal axis coordinate system, the conductivity tensor diagonalizes as

$$\boldsymbol{\sigma} = \begin{bmatrix} \sigma_x & 0 & 0 \\ 0 & \sigma_y & 0 \\ 0 & 0 & \sigma_z \end{bmatrix}. \tag{1}$$

For an isotropic medium, the conductivity is a scalar, i.e., $\sigma_x = \sigma_y = \sigma_z = a$; for a transversely isotropic (TI) medium, two of the three principal conductivities are equal. On the scale of logging measurements, thin-bedded sand-shale sequences frequently exhibit transverse isotropy, i.e., $\sigma_x = \sigma_y$. If a layered medium has a fracture pattern that cuts across bedding, the conductivity is fully anisotropic. Full anisotropy is referred to as biaxial anisotropy in crystals. In this case, all three principal conductivities are different, representing the differences of pore connectivity and conductivity in vertical and lateral directions.

Traditional induction tools have only coaxial transmitter-receiver coils and measure one magnetic-field component at different receiver locations. To characterize anisotropic conductivity, conventional induction-logging methods must be extended to provide additional information. Multicomponent induction-logging tools (Kriegshäuser et al., 2000; Anderson et al., 2002; Rosthal et al., 2003; Zhang et al., 2004; Rabinovich et al., 2006; Wang et al., 2006;

Manuscript received by the Editor 7 April 2009; revised manuscript received 2 September 2009; published online 5 April 2010.
[1]University of Houston, Department of Electrical and Computer Engineering, Houston, Texas, U.S.A. E-mail: nyuan@uh.edu; xnie@uh.edu; cliu@uh.edu.
[2]National University of Singapore, Department of Electrical and Computer Engineering, Singapore. E-mail: cwqiu@nus.edu.sg.

Rabinovich et al., 2007; Davydycheva et al., 2009) are designed to obtain formation anisotropy. The rich information provided by multicomponent induction measurements determines complex formations such as biaxial anisotropic media.

In this paper, we consider a triaxial induction tool that includes three orthogonal transmitters and three orthogonal receivers, as shown in Figure 1 (Anderson et al., 2002). The study of the impact of anisotropy on the tool's response is important for the correct interpretation of measurements. Among various studies on electrical anisotropy, most studies assumed a TI or uniaxial medium for convenience (Chetaev, 1966; Althausen, 1969; Moran and Gianzero, 1979, 1982; Chemali et al., 1987; Lüling et al., 1994; Anderson et al., 1995; Wang et al., 2003; Zhang et al., 2004; Wang et al., 2006; Lee and Teixeira, 2007; Zhong et al., 2008). Although transverse isotropy is a reasonable approximation based on stratigraphic geometry, the assumption is made primarily for mathematical convenience rather than for its low frequency of occurrence in nature because Maxwell's equations can be solved analytically, leading to relatively simple formulas for a TI medium.

The likelihood of encountering biaxial anisotropy in sedimentary rocks has been reported by Sawyer et al. (1971), Zafran (1981), and Zhao et al. (1994), and interest in studying tool response in a biaxial

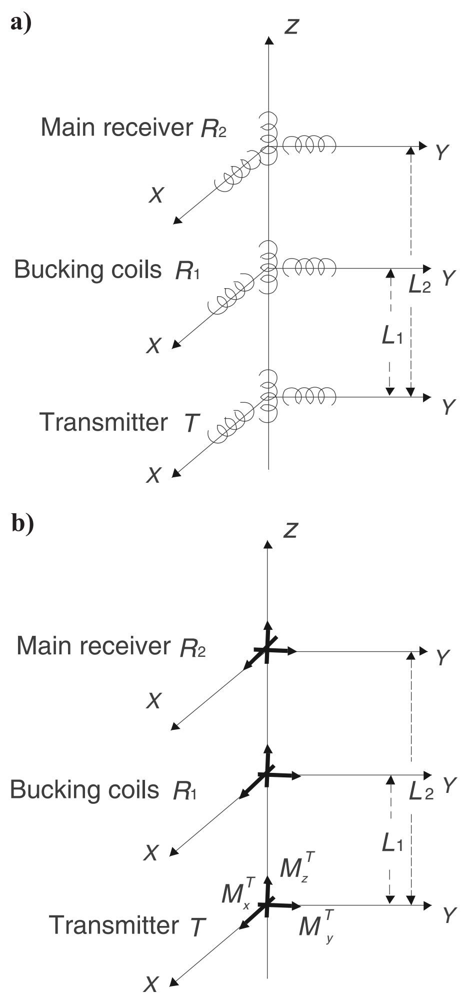

Figure 1. (a) Basic structure of a triaxial induction tool and (b) its equivalent dipole model.

anisotropic medium is increasing. However, because of mathematical complexity, there are few theoretical studies on biaxial anisotropy (Nekut, 1994; Gianzero et al., 2002). Nekut (1994), in the first theoretical work on biaxial anisotropy, considers the response of a hypothetical time-domain instrument with a zero-spacing transmitter and receiver in a biaxial medium. Gianzero et al. (2002) study the response of a triaxial induction instrument in a biaxial anisotropic medium. Different from Nekut's work, Gianzero et al. (2002) consider nonzero spacing between the three orthogonal transmitters and three orthogonal receivers. Also, their analysis is in the frequency domain instead of the time domain. The work of Gianzero et al. lays the foundation to the response of triaxial induction logging tools in a biaxial anisotropic formation. However, they only consider a special case where the instrument is oriented parallel to the principal axes of a biaxial medium. In practice, the instrument can be oriented arbitrarily with respect to the principal axes of the biaxial medium, complicating the forward-modeling problem.

Here, we study the response of a triaxial induction sonde in a more general case where the coil axes of the instrument are arbitrarily rotated and/or tilted with respect to the conductivity tensor principal axes of the biaxial anisotropic medium. We further extend the method of Gianzero et al. (2002) to derive the formulas for computing the magnetic-field responses. The full coupling matrix connecting the source excitations to the magnetic-field response is presented, and the critical numerical methods are discussed. Numerical examples are presented to validate formulations and numerical evaluation. The sensitivity of tool responses to factors such as dipping, azimuthal and tool angles, and frequency are also investigated.

FORMULATION

In this section, we will derive the magnetic-field response of a triaxial tool in a biaxial anisotropic medium and discuss the evaluation of the inverse Fourier transform.

Spectral-domain solution to Maxwell's equations in a homogeneous biaxial anisotropic medium

A homogeneous, biaxial, unbounded medium can be characterized by the tensor conductivity defined in equation 1 (expressed in the principal axis system). Assuming the harmonic time dependence to be $e^{-i\omega t}$ (suppressed throughout our paper), Maxwell's equations for the electric and magnetic fields are

$$\nabla \times \mathbf{H}(\mathbf{r}) = (\boldsymbol{\sigma} - i\omega\boldsymbol{\varepsilon})\mathbf{E}(\mathbf{r}) + \mathbf{J}_s(\mathbf{r}), \tag{2a}$$

$$\nabla \times \mathbf{E}(\mathbf{r}) = i\omega\mu_0\mathbf{H}(\mathbf{r}) + i\omega\mu_0\mathbf{M}_s(\mathbf{r}), \tag{2b}$$

where μ_0 is the magnetic permeability of the air, $\mathbf{r} = (x,y,z)$ is the position vector, $\boldsymbol{\varepsilon}$ is the dielectric constant tensor, $\mathbf{M}_s(\mathbf{r})$ is the magnetic-source flux density, and $\mathbf{J}_s(\mathbf{r})$ is the electric source current density.

For logging devices operating at relatively low frequencies and formations with conductivities greater than 10^{-4} S/m, we can assume that contributions from displacement current determined by $i\omega\boldsymbol{\varepsilon}$ can be ignored in comparison with $\boldsymbol{\sigma}$. For the induction logging problems considered in this paper, we assume that $\mathbf{J}_s(\mathbf{r}) = 0$, which means only magnetic dipoles are used to represent induction coils. Therefore, Maxwell's equations are reduced to

$$\nabla \times \mathbf{H}(\mathbf{r}) = \boldsymbol{\sigma}\mathbf{E}(\mathbf{r}), \tag{3a}$$

$$\nabla \times \mathbf{E}(\mathbf{r}) = i\omega\mu_0\mathbf{H}(\mathbf{r}) + i\omega\mu_0\mathbf{M}_s(\mathbf{r}). \tag{3b}$$

The solution for equation 3 in the space domain can be expressed in terms of triple Fourier transforms of their spectral-domain counterparts $\tilde{\mathbf{E}}(\mathbf{k})$ and $\tilde{\mathbf{H}}(\mathbf{k})$:

$$E(\mathbf{r}),\mathbf{H}(\mathbf{r}) = \frac{1}{(2\pi)^3}\int_{\mathbf{k}} d\mathbf{K}e^{i\mathbf{K}\cdot\mathbf{r}}\tilde{\mathbf{E}}(\mathbf{K}),\tilde{\mathbf{H}}(\mathbf{K}), \tag{4}$$

where $\mathbf{K} = (\xi, \eta, \varsigma)$ and where

$$\tilde{\mathbf{E}}(\mathbf{K}),\tilde{\mathbf{H}}(\mathbf{K}) = \int_{\mathbf{r}} dre^{-i\mathbf{K}\cdot\mathbf{r}}\mathbf{E}(\mathbf{r}),\mathbf{H}(\mathbf{r}) \tag{5}$$

and

$$\int_{k} d\mathbf{K}e^{i\mathbf{K}\cdot\mathbf{r}} = \int_{-\infty}^{\infty}\int_{-\infty}^{\infty}\int_{-\infty}^{\infty} d\xi d\eta d\varsigma e^{i(\xi x + \eta y + \varsigma z)}. \tag{6}$$

Thus, for mathematical convenience, we first solve equation 3 in the spectral domain and then use equation 4 to obtain the space-domain solutions from their spectral-domain counterparts.

For the spectral-domain solutions $\tilde{\mathbf{E}}(\mathbf{K})$ and $\tilde{\mathbf{H}}(\mathbf{K})$, we can first eliminate the magnetic fields using electric fields in equation 3a and solve for $\tilde{\mathbf{E}}(\mathbf{K})$ from equation 3b in the presence of the source $\mathbf{M}_s(\mathbf{r})$. Then, because the source singularity has been totally accounted for in this solution, the magnetic fields can be determined from a homogeneous form of Maxwell's equations.

Substituting equation 3a and 3b results in the following vector wave equation:

$$\nabla\nabla\cdot\mathbf{E}(\mathbf{r}) - \nabla^2\mathbf{E}(\mathbf{r}) - \mathbf{k}^2\mathbf{E}(\mathbf{r}) = i\omega\mu\nabla\times\mathbf{M}_s(\mathbf{r}), \tag{7}$$

where $\mathbf{k}^2 = i\omega\mu_0\boldsymbol{\sigma}$. Applying the triple Fourier transform defined in equation 6 and equation 7, we obtain

$$\boldsymbol{\Omega}(\mathbf{K})\cdot\tilde{\mathbf{E}}(\mathbf{K}) = -i\omega\mu\nabla\times\mathbf{M}_s(\mathbf{K}), \tag{8}$$

where the coefficient matrix $\boldsymbol{\Omega}$ is given by

$$\boldsymbol{\Omega} = \begin{bmatrix} k_x^2 - (\eta^2 + \varsigma^2) & \xi\eta & \xi\varsigma \\ \xi\eta & k_y^2 - (\xi^2 + \varsigma^2) & \eta\varsigma \\ \xi\varsigma & \eta\varsigma & k_z^2 - (\xi^2 + \eta^2) \end{bmatrix}. \tag{9}$$

Then, the solutions for the space-domain fields are

$$\mathbf{E}(\mathbf{r}) = -\frac{i\omega\mu}{(2\pi)^3}\int_{\mathbf{K}} d\mathbf{K}e^{i\mathbf{K}\cdot\mathbf{r}}\boldsymbol{\Omega}^{-1}(\mathbf{K})\nabla\times\mathbf{M}_s(\mathbf{K}). \tag{10}$$

The inverse matrix $\boldsymbol{\Omega}^{-1}$ can be computed in terms of its adjoint and determinant as

$$\boldsymbol{\Omega}^{-1} = \frac{\Lambda}{\det\boldsymbol{\Omega}}. \tag{11}$$

Let $\omega_{ij}(i = 1,2,3;\ j = 1,2,3)$ denote element (i,j) in the inverse matrix. The elements are found to be

$$\omega_{11} = \frac{[k_y^2 - (\xi^2 + \varsigma^2)][k_z^2 - (\xi^2 + \eta^2)] - \eta^2\varsigma^2}{\det\boldsymbol{\Omega}}, \tag{12a}$$

$$\omega_{12} = \omega_{21} = \frac{-\xi\eta[k_z^2 - (\xi^2 + \eta^2 + \varsigma^2)]}{\det\boldsymbol{\Omega}}, \tag{12b}$$

$$\omega_{13} = \omega_{31} = \frac{-\xi\varsigma[k_y^2 - (\xi^2 + \eta^2 + \varsigma^2)]}{\det\boldsymbol{\Omega}}, \tag{12c}$$

$$\omega_{22} = \frac{[k_x^2 - (\eta^2 + \varsigma^2)][k_z^2 - (\xi^2 + \eta^2)] - \xi^2\varsigma^2}{\det\boldsymbol{\Omega}}, \tag{12d}$$

$$\omega_{23} = \omega_{32} = \frac{-\eta\varsigma[k_x^2 - (\xi^2 + \eta^2 + \varsigma^2)]}{\det\boldsymbol{\Omega}}, \tag{12e}$$

$$\omega_{33} = \frac{[k_x^2 - (\eta^2 + \varsigma^2)][k_y^2 - (\xi^2 + \varsigma^2)] - \xi^2\eta^2}{\det\boldsymbol{\Omega}}. \tag{12f}$$

The determinant of the coefficient matrix can be written in the following factored form:

$$\det\boldsymbol{\Omega} = k_z^2(\varsigma^2 - \varsigma_o^2)(\varsigma^2 - \varsigma_e^2), \tag{13}$$

where ς_o and ς_e are the axial wavenumbers of the ordinary and extraordinary modes of propagation. The two distinct modes of propagation can be found to be (Appendix A)

$$\varsigma_{o,e}^2 = a \pm \sqrt{b}, \tag{14}$$

where

$$a = \frac{k_z^2(k_x^2 + k_y^2) - \xi^2(k_x^2 + k_z^2) - \eta^2(k_y^2 + k_z^2)}{2k_z^2} \tag{15}$$

and

$$b = a^2 - \frac{(\xi^2 + \eta^2 - k_z^2)(\xi^2k_x^2 + \eta^2k_y^2 - k_x^2k_y^2)}{k_z^2}. \tag{16}$$

The positive and negative square roots correspond to ς_e and ς_o, respectively. Our derivation (equations 7–16) follows that of Gianzero et al. (2002) but modifies all typographical errors. Detailed derivation of a and b can be found in Appendix A.

Once the space-domain electric field is obtained from equation 10, the corresponding magnetic field can be determined from the source-free Maxwell equations.

Full magnetic-field response of triaxial induction sonde in biaxial anisotropic medium

In this section, we derive the full magnetic-field response of a triaxial induction sonde in a biaxial anisotropic medium. The basic structure of a triaxial tool is shown in Figure 1a, consisting of one group of transmitter coils, one group of bucking coils, and one group of receiver coils. All transmitter, bucking, and receiver coils are oriented in three mutually orthogonal directions. In the analysis, the coils are assumed to be sufficiently small and replaced by point magnetic dipoles in the modeling. Thus, the magnetic-source excitation of the triaxial tool can be expressed as $\mathbf{M}=(M_x,M_y,M_z)\delta(\mathbf{r})$, as shown in Figure 1b.

For each component of the transmitter moments M_x, M_y, and M_z, there generally are three components of the induced field at each point in the medium. Thus, there are nine field components at each receiver location. These field components can be expressed by a matrix representation of a dyadic $\hat{\mathbf{H}}$ as

$$\hat{\mathbf{H}}=\begin{bmatrix} H_{xx} & H_{xy} & H_{xz}\\ H_{yx} & H_{yy} & H_{yz}\\ H_{zx} & H_{zy} & H_{zz}\end{bmatrix}, \tag{17}$$

where the first subscript corresponds to the transmitter index and the second corresponds to the receiver index. Therefore, H_{ij} denotes the magnetic field received by the j-directed receiver coil excited by the i-directed transmitter coil.

Next, we derive the expressions for the nine magnetic-field components in a homogeneous biaxial medium.

Magnetic-field components generated by a unit x-directed magnetic dipole $\mathbf{M}=(1,0,0)^T$

For an x-directed magnetic dipole $\mathbf{M}=(1,0,0)^T$ located at $\mathbf{r}'=(x',y',z')$, equation 8 can be rewritten as

$$\mathbf{\Omega}(\mathbf{K})\cdot\begin{bmatrix}\tilde{E}_{xx}(\mathbf{K})\\ \tilde{E}_{xy}(\mathbf{K})\\ \tilde{E}_{xz}(\mathbf{K})\end{bmatrix}=\omega\mu_0 e^{-i(\xi x'+\eta y'+\varsigma z')}\begin{bmatrix}0\\ \varsigma\\ -\eta\end{bmatrix}. \tag{18}$$

Solving equation 18, we can get

$$\begin{bmatrix}\tilde{E}_{xx}(\mathbf{K})\\ \tilde{E}_{xy}(\mathbf{K})\\ \tilde{E}_{xz}(\mathbf{K})\end{bmatrix}=\omega\mu_0 e^{-i(\xi x'+\eta y'+\varsigma z')}\begin{bmatrix}\varsigma\omega_{12}-\eta\omega_{13}\\ \varsigma\omega_{22}-\eta\omega_{23}\\ \varsigma\omega_{32}-\eta\omega_{33}\end{bmatrix}. \tag{19}$$

The corresponding components of the magnetic field can be determined from the source-free Maxwell equations:

$$\tilde{H}_x=\frac{1}{\omega\mu_0}(\eta\tilde{E}_z-\varsigma\tilde{E}_y), \tag{20a}$$

$$\tilde{H}_y=\frac{1}{\omega\mu_0}(\varsigma\tilde{E}_x-\xi\tilde{E}_z), \tag{20b}$$

$$\tilde{H}_z=\frac{1}{\omega\mu_0}(\xi\tilde{E}_y-\eta\tilde{E}_x). \tag{20c}$$

Direct substitution of equation 19 into equation 20 yields

$$\begin{bmatrix}\tilde{H}_{xx}(\mathbf{K})\\ \tilde{H}_{xy}(\mathbf{K})\\ \tilde{H}_{xz}(\mathbf{K})\end{bmatrix}=e^{-i(\xi x'+\eta y'+\varsigma z')}\cdot\begin{bmatrix}\eta(\varsigma\omega_{32}-\eta\omega_{33})-\varsigma(\varsigma\omega_{22}-\eta\omega_{23})\\ \varsigma(\varsigma\omega_{12}-\eta\omega_{13})-\xi(\varsigma\omega_{32}-\eta\omega_{33})\\ \xi(\varsigma\omega_{22}-\eta\omega_{23})-\eta(\varsigma\omega_{12}-\eta\omega_{13})\end{bmatrix}. \tag{21}$$

Then, the magnetic-field components in the space domain can be obtained from their spectral-domain counterparts in equation 21 by applying inverse Fourier transforms defined in equation 6:

$$H_{xx}(\mathbf{r})=\frac{1}{(2\pi)^3}\int_{-\infty}^{\infty}\int_{-\infty}^{\infty}\int_{-\infty}^{\infty}d\xi d\eta d\varsigma\cdot e^{i\xi(x-x')}e^{i\eta(y-y')}e^{i\varsigma(z-z')}(2\eta\varsigma\omega_{23}-\eta^2\omega_{33}-\varsigma^2\omega_{22}), \tag{22}$$

$$H_{xy}(\mathbf{r})=\frac{1}{(2\pi)^3}\int_{-\infty}^{\infty}\int_{-\infty}^{\infty}\int_{-\infty}^{\infty}d\xi d\eta d\varsigma e^{i\xi(x-x')}ei\eta(y-y')\cdot e^{i\varsigma(z-z')}[\varsigma(\varsigma\omega_{12}-\eta\omega_{13})-\xi(\varsigma\omega_{32}-\eta\omega_{33})], \tag{23}$$

$$H_{xz}(\mathbf{r})=\frac{1}{(2\pi)^3}\int_{-\infty}^{\infty}\int_{-\infty}^{\infty}\int_{-\infty}^{\infty}d\xi d\eta d\varsigma e^{i\xi(x-x')}\cdot e^{i\eta(y-y')}e^{i\varsigma(z-z')}[\xi(\varsigma\omega_{22}-\eta\omega_{23})-\eta(\varsigma\omega_{12}-\eta\omega_{13})]. \tag{24}$$

As can be seen from equations 22–24, triple infinite integrals of x, y, and z are involved in the solution. In the numerical evaluation, a cylindrical transformation in the wavenumber space is invoked. Let ψ be the rotation angle in the $\xi-\eta$-plane, and we have

$$\xi=k\cos\psi, \tag{25a}$$

$$\eta=k\sin\psi, \tag{25b}$$

$$\int_{-\infty}^{\infty}\int_{-\infty}^{\infty}\int_{-\infty}^{\infty}d\xi d\eta d\varsigma=\int_0^{2\pi}d\psi\int_0^{\infty}kdk\int_{-\infty}^{\infty}d\varsigma. \tag{25c}$$

Thus, equations 22–24 can be rewritten as

$$H_{xx}(\mathbf{r})=\frac{1}{(2\pi)^3}\int_0^{2\pi}d\psi\int_0^{\infty}kdk\int_{-\infty}^{\infty}d\varsigma\cdot e^{ik\cos\psi(x-x')}e^{ik\sin\psi(y-y')}e^{i\varsigma(z-z')}\cdot(2k\varsigma\sin\psi\omega_{32}-k^2\sin^2\psi\omega_{33}-\varsigma^2\omega_{22}), \tag{26}$$

$$H_{xy}(r) = \frac{1}{(2\pi)^3}\int_0^{2\pi} d\psi \int_0^{\infty} k dk \int_{-\infty}^{\infty} d\varsigma \cdot e^{ik\cos\psi(x-x')}e^{ik\sin\psi(y-y')}e^{i\varsigma(z-z')} \cdot(\varsigma^2\omega_{12} - k\varsigma\sin\psi\omega_{13} - k\varsigma\cos\psi\omega_{32} + k^2\cos\psi\sin\psi\omega_{33}), \quad (27)$$

$$H_{xz}(r) = \frac{1}{(2\pi)^3}\int_0^{2\pi} d\psi \int_0^{\infty} dk k^2 \int_{-\infty}^{\infty} d\varsigma \cdot e^{ik\cos\psi(x-x')}e^{ik\sin\psi(y-y')}e^{i\varsigma(z-z')} \cdot (k\sin^2\psi\omega_{13} - k\sin\psi\cos\psi\omega_{23} - \varsigma\sin\psi\omega_{12} + \varsigma\cos\psi\omega_{22}). \quad (28)$$

Magnetic-field components generated by a unit y*-directed magnetic dipole* $\mathbf{M} = (0,1,0)^T$

For a y-directed magnetic dipole $\mathbf{M} = (0,1,0)^T$ at $\mathbf{r}' = (x',y',z')$, following a similar derivation procedure, we can obtain the solution for the space-domain magnetic field components as follows:

$$H_{yx}(\mathbf{r}) = \frac{1}{(2\pi)^3}\int_{-\infty}^{\infty}\int_{-\infty}^{\infty}\int_{-\infty}^{\infty} d\xi d\eta d\varsigma \cdot e^{i\xi(x-x')}e^{i\eta(y-y')}e^{i\varsigma(z-z')}[\eta(\xi\omega_{33} - \varsigma\omega_{31}) - \varsigma(\xi\omega_{23} - \varsigma\omega_{21})], \quad (29)$$

$$H_{yy}(\mathbf{r}) = \frac{1}{(2\pi)^3}\int_{-\infty}^{\infty}\int_{-\infty}^{\infty}\int_{-\infty}^{\infty} d\xi d\eta d\varsigma \cdot e^{i\xi(x-x')}e^{i\eta(y-y')}e^{i\varsigma(z-z')} \cdot(2\varsigma\xi\omega_{13} - \varsigma^2\omega_{11} - \xi^2\omega_{33}), \quad (30)$$

$$H_{yz}(\mathbf{r}) = \frac{1}{(2\pi)^3}\int_{-\infty}^{\infty}\int_{-\infty}^{\infty}\int_{-\infty}^{\infty} d\xi d\eta d\varsigma \cdot e^{i\xi(x-x')}e^{i\eta(y-y')}e^{i\varsigma(z-z')}[\xi(\xi\omega_{23} - \varsigma\omega_{21}) - \eta(\xi\omega_{13} - \varsigma\omega_{11})]. \quad (31)$$

Equations 32–34 are actually used in the numerical evaluation by transforming the Cartesian coordinates into cylindrical coordinates:

$$H_{yx}(\mathbf{r}) = \frac{1}{(2\pi)^3}\int_0^{2\pi} d\psi \int_0^{\infty} dk k \int_{-\infty}^{\infty} d\varsigma e^{ik\cos\psi(x-x')} \cdot e^{ik\sin\psi(y-y')}e^{i\varsigma(z-z')} \cdot(\varsigma^2\omega_{21} - k\varsigma\sin\psi\omega_{31} - k\varsigma\cos\psi\omega_{23} + k^2\cos\psi\sin\psi\omega_{33}), \quad (32)$$

$$H_{yy}(\mathbf{r}) = \frac{1}{(2\pi)^3}\int_0^{2\pi} d\psi \int_0^{\infty} dk k \int_{-\infty}^{\infty} d\varsigma e^{ik\cos\psi(x-x')} \cdot e^{ik\sin\psi(y-y')}e^{i\varsigma(z-z')}(2k\varsigma\cos\psi\omega_{13} - k^2\cos^2\psi\omega_{33} - \varsigma^2\omega_{11}), \quad (33)$$

$$H_{yz}(\mathbf{r}) = \frac{1}{(2\pi)^3}\int_0^{2\pi} d\psi \int_0^{\infty} dk k^2 \int_{-\infty}^{\infty} d\varsigma e^{ik\cos\psi(x-x')} \cdot e^{ik\sin\psi(y-y')}e^{i\varsigma(z-z')} \cdot(\varsigma\sin\psi\omega_{11} - \varsigma\cos\psi\omega_{21} - k\cos\psi\sin\psi\omega_{13} + k\cos^2\psi\omega_{23}). \quad (34)$$

Note that H_{yx} has the same expression as H_{xy}. This is because of the reciprocity of the medium. We see in the following equations that H_{xz} and H_{zx} as well as H_{yz} and H_{zy} have the same expression because of reciprocity.

Magnetic-field components generated by a unit z*-directed magnetic dipole* $\mathbf{M} = (0,0,1)^T$

Similarly, for a z-directed magnetic dipole $\mathbf{M} = (0,0,1)^T$ at $\mathbf{r}' = (x',y',z')$, the magnetic fields in the space domain are

$$H_{zx}(\mathbf{r}) = \frac{1}{(2\pi)^3}\int_{-\infty}^{\infty}\int_{-\infty}^{\infty}\int_{-\infty}^{\infty} d\xi d\eta d\varsigma \cdot e^{i\xi(x-x')}e^{i\eta(y-y')}e^{i\varsigma(z-z')}[\eta(\eta\omega_{31} - \xi\omega_{32}) - \varsigma(\eta\omega_{21} - \xi\omega_{22})], \quad (35)$$

$$H_{zy}(\mathbf{r}) = \frac{1}{(2\pi)^3}\int_{-\infty}^{\infty}\int_{-\infty}^{\infty}\int_{-\infty}^{\infty} d\xi d\eta d\varsigma e^{i\xi(x-x')}e^{i\eta(y-y')} \cdot e^{i\varsigma(z-z')}[\varsigma(\eta\omega_{11} - \xi\omega_{12}) - \xi(\eta\omega_{31} - \xi\omega_{32})], \quad (36)$$

$$H_{zz}(\mathbf{r}) = \frac{1}{(2\pi)^3}\int_{-\infty}^{\infty}\int_{-\infty}^{\infty}\int_{-\infty}^{\infty} d\xi d\eta d\varsigma \cdot e^{i\xi(x-x')}e^{i\eta(y-y')}e^{i\varsigma(z-z')}[\xi(\eta\omega_{21} - \xi\omega_{22}) - \eta(\eta\omega_{11} - \xi\omega_{12})]. \quad (37)$$

Transforming the integral variables ξ and η into k and ψ, we have

$$H_{zx}(\mathbf{r}) = \frac{1}{(2\pi)^3}\int_0^{2\pi} d\psi \int_0^{\infty} dk k^2 \int_{-\infty}^{\infty} d\varsigma e^{ik\cos\psi(x-x')} \cdot e^{ik\sin\psi(y-y')}e^{i\varsigma(z-z')} \cdot (k\sin^2\psi\omega_{31} - k\sin\psi\cos\psi\omega_{32} - \varsigma\sin\psi\omega_{21} + \varsigma\cos\psi\omega_{22}), \quad (38)$$

$$H_{zy}(\mathbf{r}) = \frac{1}{(2\pi)^3}\int_0^{2\pi} d\psi \int_0^{\infty} dk k^2 \int_{-\infty}^{\infty} d\varsigma e^{ik\cos\psi(x-x')} \cdot e^{ik\sin\psi(y-y')}e^{i\varsigma(z-z')} \cdot(\varsigma\sin\psi\omega_{11} - \varsigma\cos\psi\omega_{12} - k\cos\psi\sin\psi\omega_{31} + k\cos^2\psi\omega_{32}), \quad (39)$$

$$H_{zz}(\mathbf{r}) = \frac{1}{(2\pi)^3}\int_0^{2\pi} d\psi \int_0^{\infty} dk k^3 \int_{-\infty}^{\infty} d\varsigma e^{ik\cos\psi(x-x')}$$

$$\cdot e^{ik\sin\psi(y-y')}e^{i\varsigma(z-z')}\cdot(2\sin\psi\cos\psi\omega_{12} - \cos^2\psi\omega_{22} - \sin^2\psi\omega_{11}). \tag{40}$$

In fact, for the case where the instrument's transducer axes are aligned parallel to the principal axes of the conductivity tensor (i.e., all dipping angles, azimuth angles, and tool angles are zero, $\alpha = \beta = \gamma = 0°$), all cross-coupling terms are zero. However, in general, the axes of the instrument are not parallel to the principal axes of the conductivity tensor, and the nondiagonal terms in the coupling matrix are not zero. Therefore, it is necessary to find out the full coupling matrix in a more general case.

Full magnetic-field response with arbitrary tool axis

In practice, the orientation of the transmitter and receiver coils are arbitrary with respect to the principal axes of the formation's conductivity tensor. In this section, we consider the magnetic-field response of a triaxial induction tool in a homogeneous biaxial anisotropic medium with an arbitrarily oriented tool axis.

Figure 2 (Zhong et al., 2008) shows the formation coordinate system described by (x,y,z) and a sonde coordinate system described by (x',y',z'). In Figure 2, α, β, and γ denote the dipping, azimuthal, and orientation angles, respectively. Angle α is the relative deviation of the instrument axis z' with respect to the z-axis of the conductivity tensor. Angle β is the angle between the projection of the instrument axis z' on the surface of the x-y-plane and the x-axis of the formation coordinate. Angle γ represents the rotation of the tool around the z'-axis.

The formation bedding (unprimed) frame can be related to the sonde (primed) frame by a rotation matrix $\mathbf{R}$, given by

$$\mathbf{R} = \begin{bmatrix} R_{11} & R_{12} & R_{13} \\ R_{21} & R_{22} & R_{23} \\ R_{31} & R_{32} & R_{33} \end{bmatrix} = \begin{bmatrix} \cos\alpha\cos\beta\cos\gamma - \sin\beta\sin\gamma & -\cos\alpha\cos\beta\sin\gamma - \sin\beta\cos\gamma & \sin\alpha\cos\beta \\ \cos\alpha\sin\beta\cos\gamma + \cos\beta\sin\gamma & -\cos\alpha\sin\beta\sin\gamma + \cos\beta\cos\gamma & \sin\alpha\sin\beta \\ -\sin\alpha\cos\gamma & \sin\alpha\sin\gamma & \cos\alpha \end{bmatrix}. \tag{41}$$

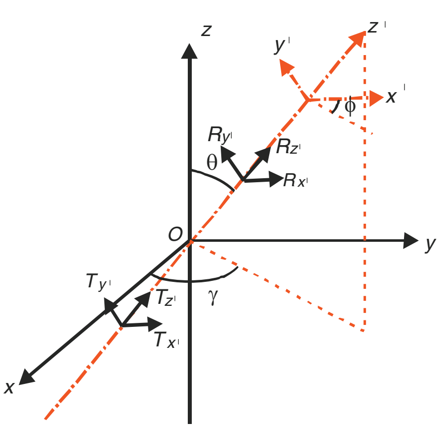

Figure 2. A schematic of the formation coordinate system (x,y,z) and sonde coordinate system (x',y',z').

To find the magnetic-field response in the sonde system, the magnetic moments of the transmitter coils in the sonde coordinates are first transformed to effective magnetic moments in the formation coordinates by the rotation matrix. Then, the magnetic fields in the formation coordinates excited by the magnetic moments $\mathbf{M}$ can be obtained readily by

$$\mathbf{H} = \hat{\mathbf{H}}\mathbf{M}, \tag{42}$$

where $\hat{\mathbf{H}}$ is the dyadic corresponding to unit dipole source given by equation 17. Once the magnetic fields at the location of the receiver coils in the formation system are determined, the magnetic fields received at the receiver coils in the sonde system can be obtained by applying the inverse of the rotation matrix (the rotation matrix is orthogonal; therefore, its inverse is equal to its transpose). Consequently, the coupling between the magnetic-field components and the magnetic dipoles in the sonde system are given by (Zhdanov et al., 2001)

$$\widehat{\mathbf{H}'} = \mathbf{R}^T\hat{\mathbf{H}}\mathbf{R}. \tag{43}$$

Computing the triple integrals

In the previous section, we obtained the expressions for all nine components of the magnetic fields. As can be seen from equations 26–28, 32–34, and 38–40, to compute the field quantities, we have to calculate integrals over k, ψ, and ς in the numerical evaluation. The integral over ψ is a definite integral, so any numerical integral method is applicable. For the semi-infinite integral over k, we use a modified Gauss-Laguerre quadrature (Burkardt, 2008). The order of Gauss-Laguerre quadrature is determined mainly by the dipping angle. Figure 3 shows the relative error of the magnetic field (imaginary part) as a function of the Gauss-Laguerre quadrature order for different dipping angles. As the dipping angle increases, a larger order of Gauss-Laguerre quadrature is required to achieve sufficient accuracy. When the dipping angle is 0°, 60°, 85°, and 89°, Gauss-Laguerre quadrature needs 16, 16, 48, and 90 points to guarantee the relative error smaller than 0.4%.

For the infinite integral of ς, the integrands become highly oscillatory as ς increases, so special integration methods must be considered. Here, the integration over ς is performed using contour integration.

From equation 13, we can see that the integrands in equations 26–28, 32–34, and 38–40 have four poles on the axial wavenumber plane: $\pm\varsigma_o$ and $\pm\varsigma_e$. The four poles correspond to the two eigenmodes for forward and backward propagation, describing the two polarizations of the electromagnetic wave in the anisotropic medium. Assume $\varsigma_o^>$ ($\varsigma_e^>$) represents the poles between ς_o (ς_e) and $-\varsigma_o(-\varsigma_e)$ whose imaginary part is greater than zero. For $z-z' > 0$, one obtains contributions only from two poles at $\varsigma_o^>$ and $\varsigma_e^>$; for $z-z' < 0$, the contributions are from two poles at $-\varsigma_o^>$ and $-\varsigma_e^>$.

Using the contour integration (Zhang and Qiu, 2001) for ς, the result of the integration over ς in equation 26 is

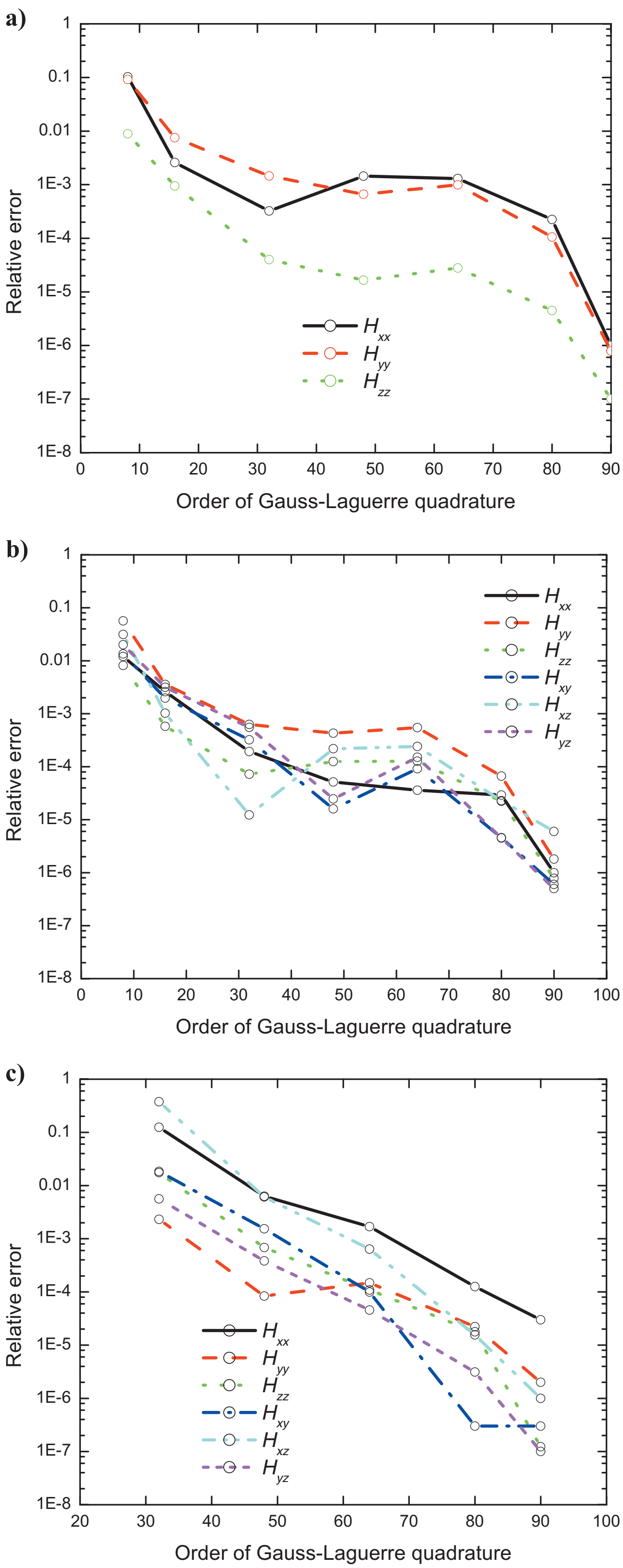

Figure 3. Relative errors as a function of Gauss-Laguerre quadrature order for different dipping angles: (a) $\alpha = 0°$, (b) $\alpha = 60°$, (c) $\alpha = 85°$.

$$\int_{-\infty}^{\infty} d\varsigma e^{i\varsigma(z-z')}(2k\varsigma\sin\psi\omega_{32} - k^2\sin^2\psi\omega_{33} - \varsigma^2\omega_{22}) = 2\pi i\cdot\Bigg\{ \frac{e^{i\varsigma(z-z')}\cdot[2k\varsigma\sin\psi\omega'_{32} - k^2\sin^2\psi\omega'_{33} - \varsigma^2\omega'_{22}]}{k_z^2(\varsigma+\varsigma_o^>)(\varsigma+\varsigma_e^>)(\varsigma-\varsigma_e^>)}\Bigg|_{\varsigma=\varsigma_o^>} + \frac{e^{i\varsigma(z-z')}\cdot[2k\varsigma\sin\psi\omega'_{32} - k^2\sin^2\psi\omega'_{33} - \varsigma^2\omega'_{22}]}{k_z^2(\varsigma+\varsigma_o^>)(\varsigma-\varsigma_o^>)(\varsigma+\varsigma_e^>)}\Bigg|_{\varsigma=\varsigma_e^>}\Bigg\}, \quad z-z'>0, \tag{44}$$

$$\int_{-\infty}^{\infty} d\varsigma e^{i\varsigma(z-z')}(2k\varsigma\sin\psi\omega_{32} - k^2\sin^2\psi\omega_{33} - \varsigma^2\omega_{22}) = 2\pi i\cdot\Bigg\{ \frac{e^{i\varsigma(z-z')}\cdot[2k\varsigma\sin\psi\omega'_{32} - k^2\sin^2\psi\omega'_{33} - \varsigma^2\omega'_{22}]}{k_z^2(\varsigma-\varsigma_o^>)(\varsigma+\varsigma_e^>)(\varsigma-\varsigma_e^>)}\Bigg|_{\varsigma=-\varsigma_o^>} + \frac{e^{i\varsigma(z-z')}\cdot[2k\varsigma\sin\psi\omega'_{32} - k^2\sin^2\psi\omega'_{33} - \varsigma^2\omega'_{22}]}{k_z^2(\varsigma+\varsigma_o^>)(\varsigma-\varsigma_o^>)(\varsigma-\varsigma_e^>)}\Bigg|_{\varsigma=-\varsigma_e^>}\Bigg\}, \quad z-z'<0, \tag{45}$$

where ω'_{32}, ω'_{33}, and ω'_{22} are the numerators of ω_{32}, ω_{33}, and ω_{22}, respectively.

Then equation 26 can be rewritten as

$$H_{xx}(\mathbf{r}) = \frac{i}{(2\pi)^2}\int_0^{2\pi} d\psi \int_0^{\infty} kdk \cdot\Bigg\{ \frac{e^{i\varsigma(z-z')}\cdot[2k\varsigma\sin\psi\omega'_{32} - k^2\sin^2\psi\omega'_{33} - \varsigma^2\omega'_{22}]}{k_z^2(\varsigma+\varsigma_o^>)(\varsigma+\varsigma_e^>)(\varsigma-\varsigma_e^>)}\Bigg|_{\varsigma=\varsigma_o^>} + \frac{e^{i\varsigma(z-z')}\cdot[2k\varsigma\sin\psi\omega'_{32} - k^2\sin^2\psi\omega'_{33} - \varsigma^2\omega'_{22}]}{k_z^2(\varsigma+\varsigma_o^>)(\varsigma-\varsigma_o^>)(\varsigma+\varsigma_e^>)}\Bigg|_{\varsigma=\varsigma_e^>}\Bigg\}, \quad z-z'>0, \tag{46}$$

$$H_{xx}(\mathbf{r}) = \frac{i}{(2\pi)^2}\int_0^{2\pi} d\psi \int_0^{\infty} kdk \cdot\Bigg\{ \frac{e^{i\varsigma(z-z')}\cdot[2k\varsigma\sin\psi\omega'_{32} - k^2\sin^2\psi\omega'_{33} - \varsigma^2\omega'_{22}]}{k_z^2(\varsigma-\varsigma_o^>)(\varsigma+\varsigma_e^>)(\varsigma-\varsigma_e^>)}\Bigg|_{\varsigma=-\varsigma_o^>} + \frac{e^{i\varsigma(z-z')}\cdot[2k\varsigma\sin\psi\omega'_{32} - k^2\sin^2\psi\omega'_{33} - \varsigma^2\omega'_{22}]}{k_z^2(\varsigma+\varsigma_o^>)(\varsigma-\varsigma_o^>)(\varsigma-\varsigma_e^>)}\Bigg|_{\varsigma=-\varsigma_e^>}\Bigg\}, \quad z-z'<0. \tag{47}$$

The integration over ς in equations 27, 28, 32–34, and 38–40 can be performed by following the same procedure. The integrands are not separable functions of k, ψ, and ς; therefore, the integrals over k, ψ, and ς cannot be performed independently.

NUMERICAL RESULTS AND DISCUSSION

In this section, we present numerical examples calculated using the Fortran code based on the present theory.

Example 1

First, we compare the apparent resistivity obtained from the present code with the available data given by Gianzero et al. (2002). For consistency with the reference, the TRI2C40 triaxial tool (distance between transmitters and receivers is 40 inches; no bucking coils) is used. The operating frequency is assumed to be 20 KHz.

The voltage responses at 20 KHz for one coaxial ($2C40_{zz}$) and two mutually perpendicular transverse, coplanar ($2C40_{xx}$,$2C40_{yy}$) arrays were converted to units of apparent conductivity. As we know, the quadrature component of the magnetic field (R-signal) is generated by currents in the formation, and the in-phase component of the field (X-signal) is not easy to observe because of the large primary field. So the signal in the air is subtracted from the signal in the biaxial formation before being converted to apparent resistivity. The formula presented by Wang et al. (2006) is used to calculate the apparent resistivity.

In Tables 1–3, a small range of resistivity tensor principal values is chosen and the corresponding apparent resistivity from the TRI2C40 triaxial tool is presented. The first three columns — ρ_x, ρ_y, and ρ_z — in each table represent the principal components of the resistivity tensor of the biaxial formation. In Tables 1 and 2, columns 4–6 present the R-signal apparent resistivity ρ_R, X-signal apparent resistivity ρ_X, and percentage difference between ρ_R and ρ_z obtained from our method. The percentage difference %diff ρ_z is computed using %diff $\rho_z = (\rho_R - \rho_z)/\rho_z$ (Gianzero et al., 2002). In columns 7–9, the results in Gianzero et al. (2002) are presented for comparison. The percentage difference between ρ_R and ρ_z should be positive because of its definition; therefore, the minus sign in Gianzero's paper is a typo that is corrected here.

In Table 3 for $2C40_{zz}$, there is an additional column (column 4) that gives the geometric mean of the horizontal resistivities $\rho_g = \sqrt{\rho_x \rho_y}$. Columns 5–7 show ρ_R, ρ_X, and the percentage difference between ρ_R and ρ_g [%diff $\rho_g = (\rho_R - \rho_g)/\rho_g$] obtained from our method. Columns 8–10 give the results in Gianzero et al. (2002).

Comparison of ρ_z and ρ_R in Tables 1 and 2 implies that the H_{xx} and H_{yy} coupling are primarily sensitive to ρ_z. This is mostly evident in the highly resistive media where skin effect has minimum impact. Comparison of ρ_R with ρ_g in Table 3 indicates that the H_{zz} coupling is primarily sensitive to the geometric mean of the horizontal resistivities. It suggests that a biaxial medium characterized by ρ_x and ρ_y is approximately equivalent to a uniaxial medium characterized by a single $\rho_h = \rho_g$, confirming Worthington's (1981) conjecture. Furthermore, the R-signal apparent resistivity becomes a better approximation of transverse resistivity as resistivity increases.

From these tables, we can see that for formations with low resistivities, the apparent resistivities obtained from our method are very close to those obtained by Gianzero et al. (2002); for formations with high resistivity, the apparent resistivities from our method are closer to the expected one. The discrepancies between the methods may be caused by the evaluation of the inverse Fourier transforms.

Gianzero et al. (2002) only consider the case where the instrument axes are parallel to the principal axes of the conductivity tensor; there are no available data for comparison of mutual coupling responses.

Example 2

To further validate the present method and quantify the numerical errors of the program, we consider isotropic and TI cases where exact solutions are available.

First, we consider a homogeneous isotropic medium with a conductivity of 500 mS/m. The relative dipping angle is 45° and the frequency is 20 KHz. We change the spacing between the transmitter and receiver coils from 10 inches to 60 inches. Figure 4a shows the axial component H_{zz} obtained from the present code and the exact solution. Although totally different methods are used, the two results are almost the same, validating our method.

Then, we consider a homogeneous TI medium with $\sigma_x = \sigma_y = 500$ mS/m and $\sigma_z = 125$ mS/m. The relative dipping angle is still 45° and the frequency is 20 KHz. Figure 4b shows the axial component H_{zz} obtained from the present code and the exact solution given by Moran and Gianzero (1979). Again, the results obtained from the two solutions are almost the same. The discrepancy begins from the sixth digit after the decimal point.

Example 3

After validating the derived formulation and the code, we study the sensitivity of a real practical three-coil tool that is similar to the 3D Explorer[SM] tool jointly developed by Baker Atlas and Shell (Kriegshäuser et al., 2000; Rabinovich et al., 2006). The tool com-

Table 1. Response of a $2C40_{xx}$ sonde in a biaxial anisotropic formation.

			Results from present method			Results in Gianzero et al. (2002)		
ρ_x	ρ_y	ρ_z	ρ_R	ρ_X	%diff ρ_z	ρ_R	ρ_X	%diff ρ_z
2	2	8	14.89	22.17	86.1	14.89	23.34	86.1
2	4	8	10.51	39.24	31.4	10.51	39.68	31.4
4	4	8	10.47	39.68	30.9	10.47	40.14	30.9
20	20	80	95.18	590.33	19.0	93.97	583.84	17.5
20	40	80	87.40	1091.56	9.25	86.6	1108.7	8.25
40	40	80	87.32	1105.43	9.15	86.5	1123.2	8.13
200	200	800	820.85	14,092	2.61	839.54	17,433	4.94
200	400	800	806.80	29,377	0.85	819.77	33,754	2.47
400	400	800	806.40	29,873	0.8	819.49	34,209	2.44
2000	2000	8000	8003.41	3,954,041	0.043	8118.4	534,262	1.48
2000	4000	8000	8000.83	1,240,184	0.0104	8059.4	1,040,553	0.74
4000	4000	8000	8000.74	1,221,581	0.00925	8058.5	1,053,855	0.73

prises one transmitter and two receivers, respectively, at 1 and 1.5 m from the transmitter. The tool response $\boldsymbol{\sigma}_a$ (apparent conductivity) is defined as

$$\boldsymbol{\sigma}_a = \begin{bmatrix} \sigma_a^{xx} & \sigma_a^{xy} & \sigma_a^{xz} \\ \sigma_a^{yx} & \sigma_a^{yy} & \sigma_a^{yz} \\ \sigma_a^{zx} & \sigma_a^{zy} & \sigma_a^{zz} \end{bmatrix}, \quad (48)$$

where σ_a^{ij} is the apparent conductivity of the jth receiver when the ith transmitter is excited. The tool response $\boldsymbol{\sigma}_a$ is a function of the relative dip angle α, azimuth angle β, and conductivity at each direction σ_x, σ_y, and σ_z. The sensitivity of $\boldsymbol{\sigma}_a$ to the dip angle, azimuth angle, and conductivities in each direction are the derivatives of the response with respect to

$$\frac{\partial \boldsymbol{\sigma}_a}{\partial \alpha}(\mathrm{mS/m/^\circ}), \quad \frac{\partial \boldsymbol{\sigma}_a}{\partial \beta}(\mathrm{mS}/m/^\circ),$$

$$\frac{\partial \boldsymbol{\sigma}_a}{\partial \sigma_x}, \quad \frac{\partial \boldsymbol{\sigma}_a}{\partial \sigma_y}, \quad \text{and} \quad \frac{\partial \boldsymbol{\sigma}_a}{\partial \sigma_z}.$$

Consider a homogeneous biaxial formation with $\sigma_x = 500$ mS/m, $\sigma_y = 250$ mS/m, and $\sigma_z = 125$ mS/m. The sensitivity of the triaxial tool to α, β, σ_x, σ_y, and σ_z is shown in Figures 5–9. In each figure, the horizontal axis is the relative dipping angle and the vertical axis is the azimuth angle. The color represents the sensitivity. Figure 5 shows sensitivity functions for all nine components. The cross pairs xy/yx, xz/zx, and yz/zy have the same sensitivity function in a homogeneous formation. Therefore, in Figures 6–9, we only show six components — xx, xy, xz, yy, yz, and zz — for length limitation.

From these figures, we can observe two things. First, apparent conductivity is more sensitive to the dipping and azimuth angle than to formation conductivities. Second, the sensitivity of the cross-cou-

Table 2. Response of a 2C40$_{yy}$ sonde in a biaxial anisotropic formation.

			Results from present method			Results in Gianzero et al. (2002)		
ρ_x	ρ_y	ρ_z	ρ_R	ρ_X	%diff ρ_z	ρ_R	ρ_X	%diff ρ_z
2	2	8	14.889	22.171	86.1	14.889	22.343	86.1
2	4	8	14.388	23.004	79.9	14.378	23.185	79.7
4	4	8	10.471	39.683	30.9	10.470	40.144	30.9
20	20	80	95.183	590.57	18.9	93.971	583.84	17.5
20	40	80	94.579	616.93	18.2	93.290	608.32	16.6
40	40	80	87.319	1106.3	9.15	86.502	1123.2	8.13
200	200	800	820.85	14,230	2.61	839.54	17,433	4.94
200	400	800	818.30	14,842	2.29	837.81	18,184	4.73
400	400	800	806.40	30,498	0.8	819.49	34,209	2.44
2000	2000	8000	8003.4	1,064,692	0.043	8118.4	534,262	1.48
2000	4000	8000	8002.7	979,117	0.034	8113.3	556,384	1.42
4000	4000	8000	8000.7	664,477	0.00875	8058.5	1,053,855	0.73

Table 3. Response of a 2C40$_{zz}$ sonde in a biaxial anisotropic formation.

				Results from present method			Results in Gianzero et al. (2002)		
ρ_x	ρ_y	ρ_z	$\rho_g = \sqrt{\rho_x \rho_y}$	ρ_R	ρ_X	%diff ρ_g	ρ_R	ρ_X	%diff ρ_g
2	2	8	2.00	2.307	17.347	15.4	2.308	17.346	15.4
2	4	8	2.83	3.200	27.835	13.1	3.200	27.730	13.2
4	4	8	4.00	4.422	47.138	10.6	4.419	46.859	10.5
20	20	80	20.00	20.836	509.26	4.18	20.888	493.15	4.44
20	40	80	28.28	29.33	862.26	3.71	29.37	798.23	3.84
40	40	80	40.00	41.272	1571.55	3.18	41.241	1375.20	3.10
200	200	800	200.00	203.30	11,540.16	1.65	202.73	15,087.83	1.36
200	400	800	282.84	286.40	17,539.70	1.26	286.19	24,513.56	1.18
400	400	800	400.00	403.10	28,849.37	0.775	403.84	42,482.95	0.961
2000	2000	8000	2000.00	2000.89	817,171.2	0.045	2008.61	471,693.0	0.430
2000	4000	8000	2828.43	2829.19	3,561,097.7	0.027	2839.05	759,772.4	0.376
4000	4000	8000	4000.00	4000.45	5,089,149	0.0113	4012.26	1,291,113	0.306

plings xz/zx and yz/zy are comparable to that of the diagonal coupling while the cross-couplings xy and yx are less sensitive.

Example 4

Finally, we investigate the effects of frequencies on the responses of the same three-coil tool in example 3. For clarity, we use resistivity instead of conductivity in this example. We consider two cases: (1) resistive formation and (2) conductive formation.

For the resistive case, we assume the resistivities of the formation are $\rho_x = 200$ ohm-m, $\rho_y = 400$ ohm-m, and $\rho_z = 800$ ohm-m. Figure 10 shows the apparent resistivity as frequency increases from 20 to 220 KHz when $\alpha = \beta = \gamma = 0°$. At a low frequency (20 KHz), the transverse components ρ_a^{xx} and ρ_a^{yy} are directly proportional to ρ_z and can reproduce ρ_z. Further, ρ_a^{xx} and ρ_a^{yy} exhibit much stronger skin effect than the conventional coaxial component ρ_a^{zz}. To compensate for this effect, measurements at lower frequencies are preferred. For higher frequencies, data at multiple frequencies must be acquired and a multifrequency skin-effect correction technique must be used. On the other hand, the coaxial component ρ_a^{zz} is less affected by the skin effect than ρ_a^{xx} and ρ_a^{yy}; ρ_a^{zz} can reflect the geometric mean of the horizontal resistivities ($\sqrt{\rho_x \rho_y}$) within the frequency range 20–220 KHz.

Figure 11 shows the apparent resistivity of the same tool for the same resistive formation at $\alpha = 75°$, $\beta = 30°$, and $\gamma = 0°$ as frequency increases from 20 to 220 KHz. Comparison of Figure 11 with Figure 10 shows that, in this case, the diagonal and cross components of the apparent resistivity are less sensitive to frequency than with zero dipping and azimuthal angles. Also, the cross terms ρ_a^{xy} and ρ_a^{xz} are negative. The apparent resistivities are inversely proportional to the induced magnetic field, so negative cross terms imply that the induced magnetic field is phase shifted 180° with respect to the transmitter current.

For a relative conductive case, the resistivities of the formation are supposed to be $\rho_x = 2$ ohm-m, $\rho_y = 4$ ohm-m, and

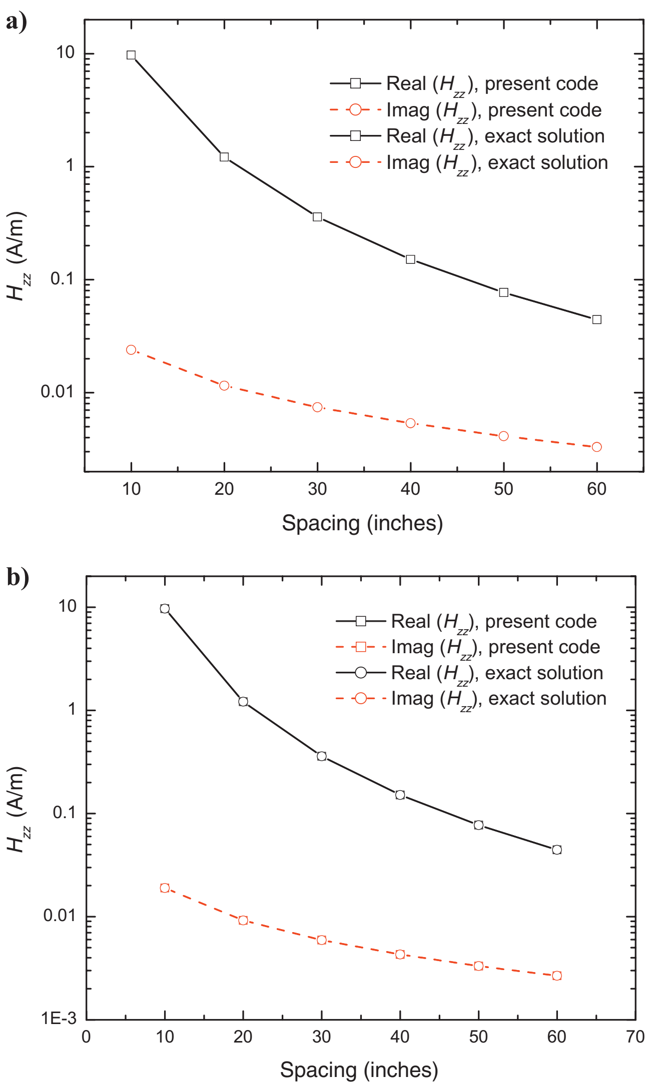

Figure 4. Comparison of the axial component H_{zz} obtained from the present code and the exact solution for (a) an isotropic medium and (b) a TI medium.

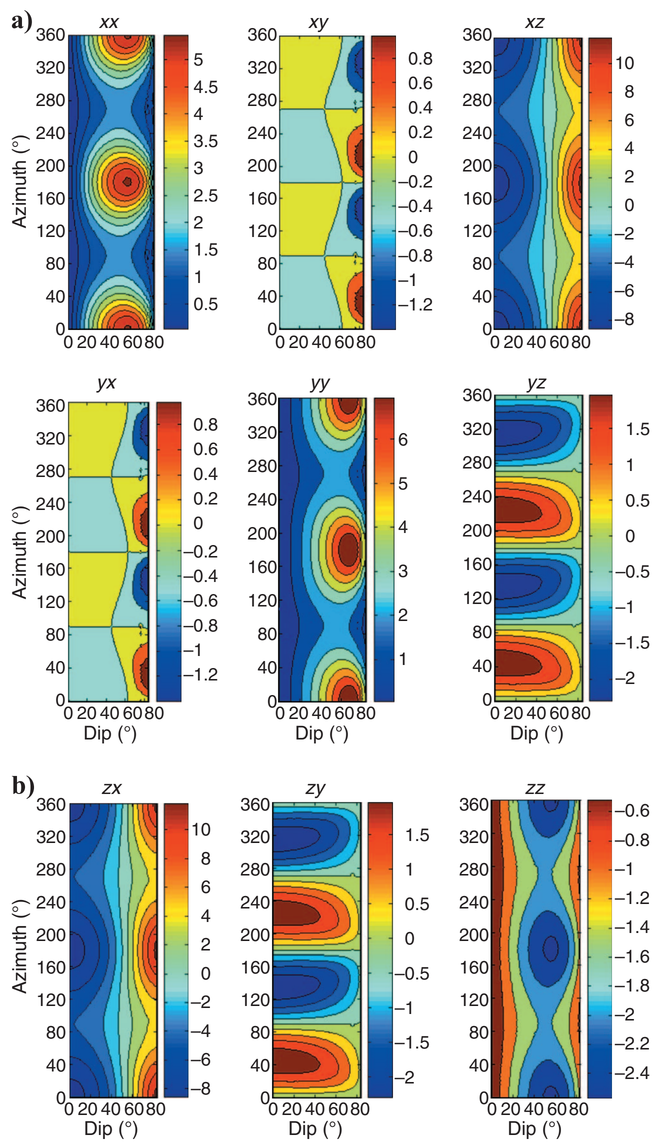

Figure 5. Sensitivity of a three-coil triaxial tool with respect to the dip angle $\partial\hat{\sigma}_a/\partial\alpha(\text{mS/m/°})$ in a homogeneous biaxial anisotropic formation.

$\rho_z = 8$ ohm-m. Figure 12 shows the apparent resistivity of the same tool for $\alpha = 60°$, $\beta = 30°$, and $\gamma = 0°$ as frequency increases from 20 to 220 KHz. All of the diagonal components of the apparent resistivity ρ_a^{xx}, ρ_a^{yy}, and ρ_a^{zz} increase as the frequency increases. As

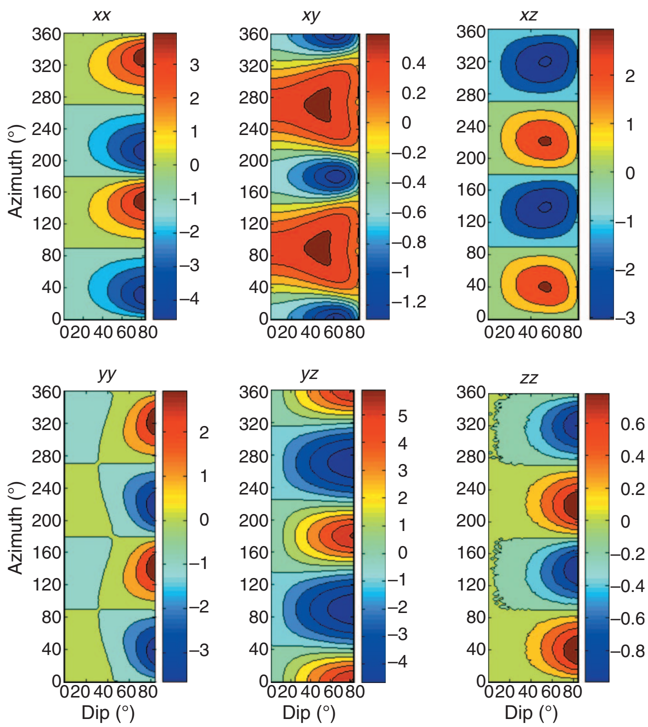

Figure 6. Sensitivity of a three-coil triaxial tool with respect to the dip angle $\partial\hat{\sigma}_a/\partial\beta(\mathrm{mS/m/°})$ in a homogeneous biaxial anisotropic formation.

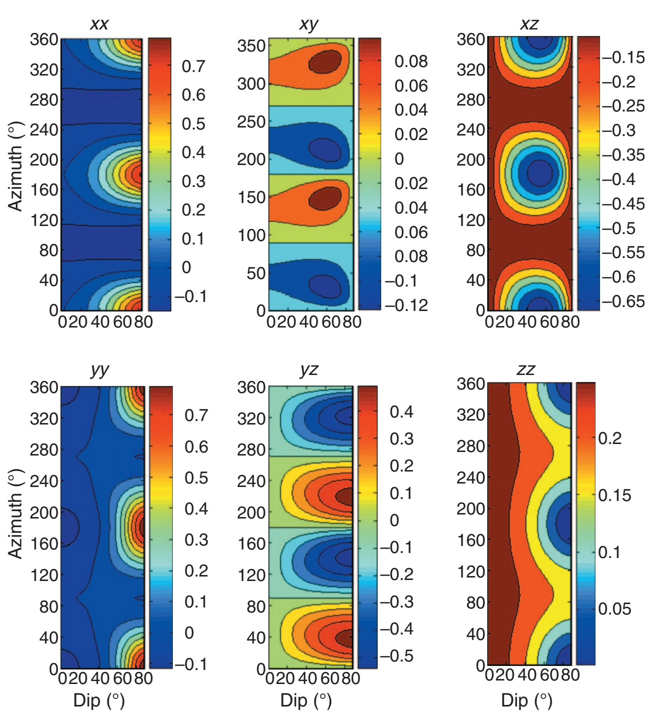

Figure 7. Sensitivity of a three-coil triaxial tool with respect to $\sigma_x(\partial\hat{\sigma}_a/\partial\sigma_x)$ in a homogeneous biaxial anisotropic formation.

for the cross components of the apparent resistivity, the amplitude (despite the phase shift with respect to the transmitter current) of ρ_a^{xz} and ρ_a^{yz} increases as the frequency increases, whereas the amplitude of ρ_a^{xy} decreases as the frequency increases. This rule also applies to the resistive case, as we can see from Figure 11.

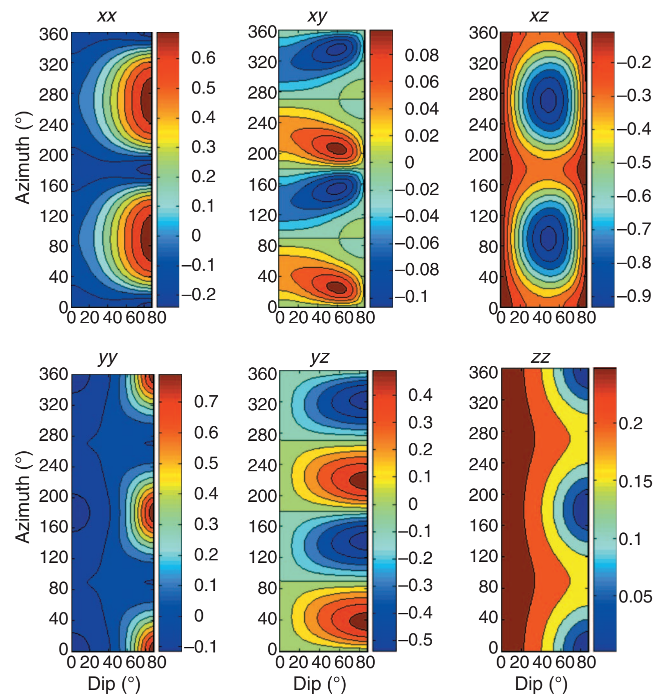

Figure 8. Sensitivity of a three-coil triaxial tool with respect to $\sigma_y(\partial\hat{\sigma}_a/\partial\sigma_y)$ in a homogeneous biaxial anisotropic formation.

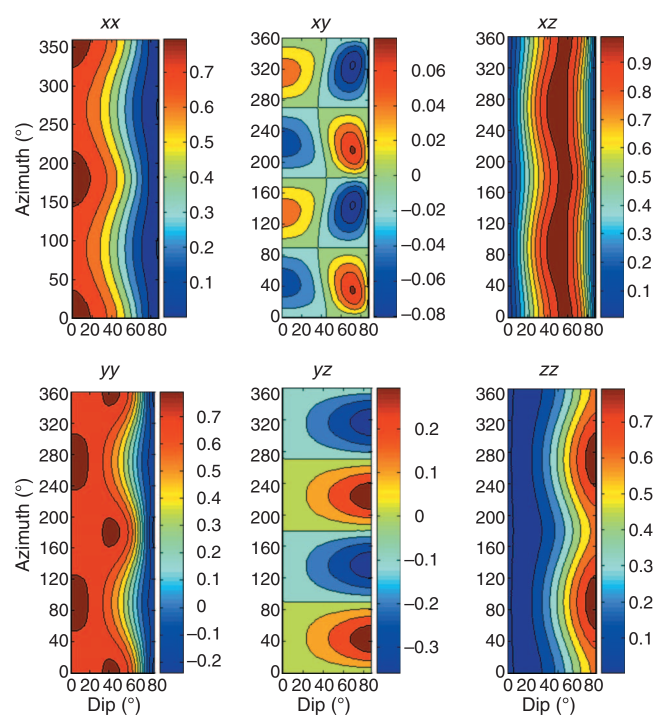

Figure 9. Sensitivity of a three-coil triaxial tool with respect to $\sigma_z(\partial\hat{\sigma}_a/\partial\sigma_z)$ in a homogeneous biaxial anisotropic formation.

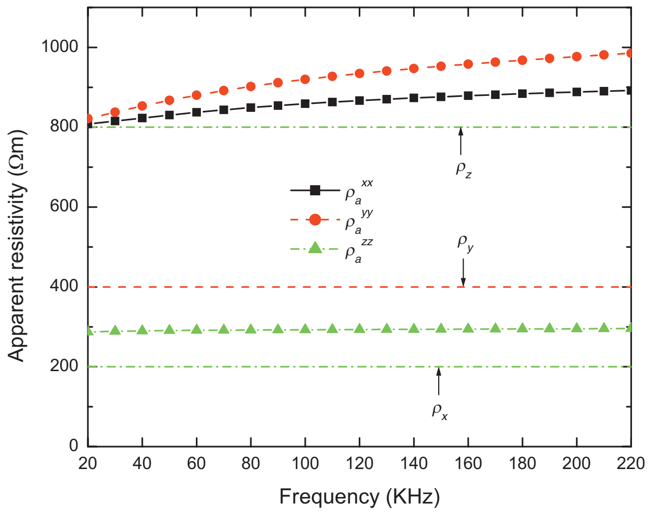

Figure 10. Frequency effect on responses of a three-coil triaxial tool in a resistive formation ($\alpha = \beta = \gamma = 0°$).

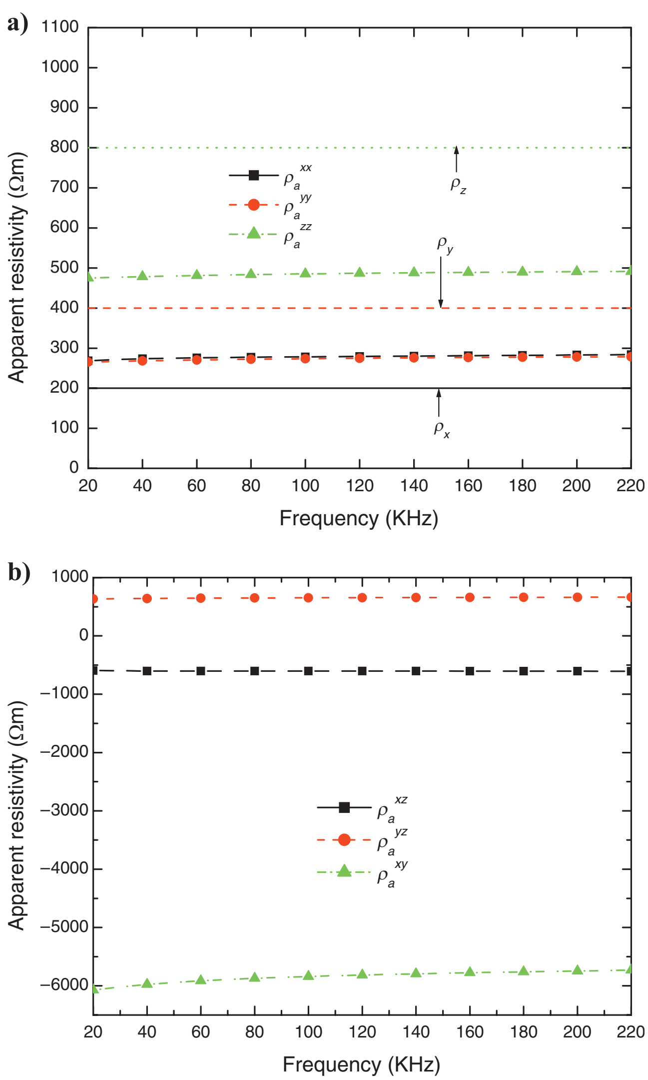

Figure 11. Frequency effect on responses of a three-coil triaxial tool in a resistive formation ($\alpha = 75°, \beta = 30°, \gamma = 0°$). (a) Diagonal term of apparent resistivity. (b) Cross terms of apparent resistivity.

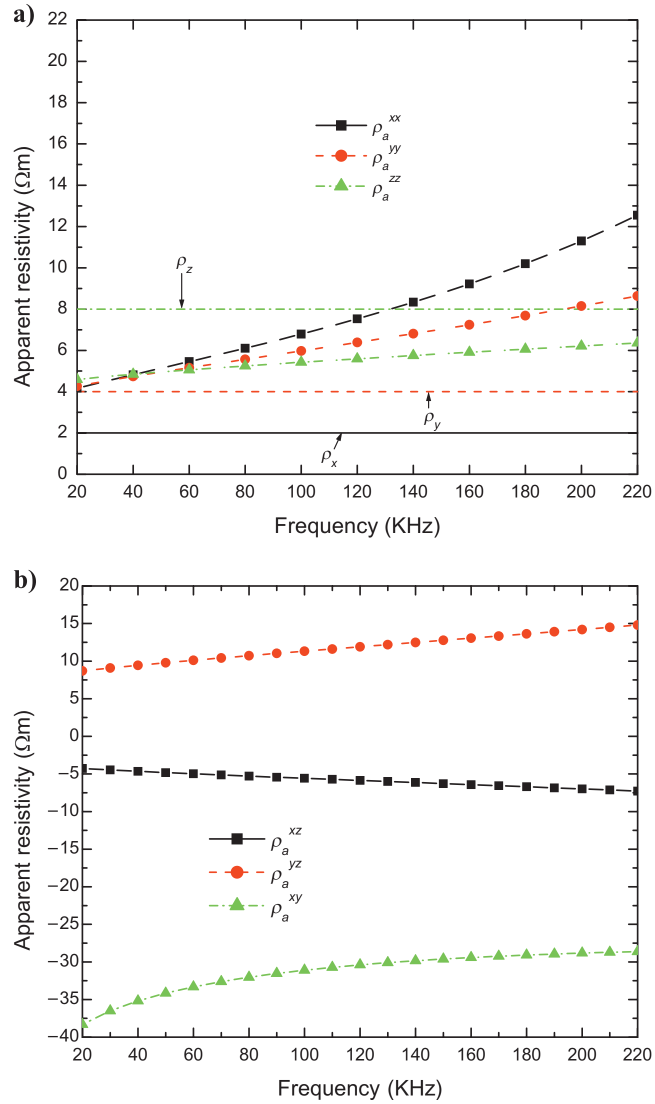

Figure 12. Frequency effect on responses of a three-coil triaxial tool in a conductive formation ($\alpha = 60°, \beta = 30°, \gamma = 0°$). (a) Diagonal term of apparent resistivity. (b) Cross terms of apparent resistivity.

Overall, our method is very efficient because it is quasi-analytical. The actual CPU time per transmitter varies with dipping angle because different numbers of integral points are required for sufficient accuracy. The general CPU time is around 10^{-2} to 10^{-1} s on a Pentium 2.4-GHz PC.

CONCLUSIONS

We have presented a theoretical analysis of the response of a triaxial induction logging tool in a homogeneous biaxial anisotropic medium. The logging tool is composed of three mutually orthogonal transmitter and receiver pairs. The axes of the transmitter and receiver can be oriented arbitrarily with respect to the principal axes of the medium's conductivity tensor. A Fortran code has been developed based on the theory, and the results are compared with the published data.

The formulas we develop are capable of analyzing cross-coupling terms, which contain information on relative deviation and relative bearing. Therefore, our formulas are more useful and practical than existing formulas because cross-coupling terms help determine the three principal components of the conductivity tensor for an arbitrarily oriented transceiver system. However, before any interpretation method can be practical, borehole effects must be corrected. Future work includes investigation of the effects of the borehole environment, such as borehole fluid, invasion, and tool eccentricity.

ACKNOWLEDGMENTS

The authors would like to acknowledge S. Gianzero for his fruitful discussion. We acknowledge the financial support of the Well Logging Industrial Consortium, which is composed of 13 oil and service companies.

APPENDIX A

DERIVATION OF PARAMETERS *a* AND *b* IN EQUATIONS 14–16

The determinant of the coefficient matrix $\mathbf{\Omega}$ can be written from equation 9 directly:

$$\det \mathbf{\Omega} = [k_x^2 - (\eta^2 + \varsigma^2)][k_y^2 - (\xi^2 + \varsigma^2)][k_z^2 - (\xi^2 + \eta^2)] + 2\xi^2\eta^2\varsigma^2 - \xi^2\varsigma^2[k_y^2 - (\xi^2 + \varsigma^2)] - \eta^2\varsigma^2[k_x^2 - (\eta^2 + \varsigma^2)] - \xi^2\eta^2[k_z^2 - (\xi^2 + \eta^2)]. \qquad \text{(A-1)}$$

By arranging the right-hand side of equation A-1 according to the mean of ς, it can be rewritten as

$$\det \mathbf{\Omega} = k_z^2\varsigma^4 - \varsigma^2[k_z^2(k_x^2 + k_y^2) - \xi^2(k_x^2 + k_z^2) - \eta^2(k_y^2 + k_z^2)] + (\xi^2 + \eta^2 - k_z^2)(\xi^2 k_x^2 + \eta^2 k_y^2 - k_x^2 k_y^2). \qquad \text{(A-2)}$$

On the other hand, from equation 13, we obtain

$$\det \mathbf{\Omega} = k_z^2\varsigma^4 - 2k_z^2\varsigma^2 a + a^2 - b. \qquad \text{(A-3)}$$

Comparing the coefficients of ς in equations A-2 and A-3 yields

$$-2k_z^2 a = -[k_z^2(k_x^2 + k_y^2) - \xi^2(k_x^2 + k_z^2) - \eta^2(k_y^2 + k_z^2)], \qquad \text{(A-4)}$$

$$a^2 - b = (\xi^2 + \eta^2 - k_z^2)(\xi^2 k_x^2 + \eta^2 k_y^2 - k_x^2 k_y^2). \qquad \text{(A-5)}$$

Therefore, the parameters a and b are

$$a = \frac{k_z^2(k_x^2 + k_y^2) - \xi^2(k_x^2 + k_z^2) - \eta^2(k_y^2 + k_z^2)}{2k_z^2} \qquad \text{(A-6)}$$

and

$$b = a^2 - \frac{(\xi^2 + \eta^2 - k_z^2)(\xi^2 k_x^2 + \eta^2 k_y^2 - k_x^2 k_y^2)}{k_z^2}. \qquad \text{(A-7)}$$

REFERENCES

Althausen, N. M., 1969, Electromagnetic wave propagation in layered-anisotropic media: Izvestia, Earth Physics, **8**, 60–69.

Anderson, B., T. Barber, and T. M. Habashy, 2002, The interpretation and inversion of fully triaxial induction data: A sensitivity study: 36th Annual Symposium, Society of Professional Well Log Analysts, Transactions, Paper O.

Anderson, B. I., T. D. Barber, and M. G. Lüling, 1995, The response of induction tools to dipping, anisotropic formations: 36th Annual Symposium, Society of Professional Well Log Analysts, Transactions, Paper D.

Burkardt, J., 2008, Quadrature rules of Gauss-Laguerre type: http://people.scs.fsu.edu/~burkardt/datasets/quadrature_rules_laguerre/quadrature_rules_laguerre.html, accessed March 2008.

Chemali, R., S. Gianzero, and S. M. Su, 1987, The effect of shale anisotropy on focused resistivity devices: 28th Annual Symposium, Society of Professional Well Log Analysts, Transactions, Paper H.

Chetaev, D. N., 1966, A new method for the solution of problems in the electrodynamics of anisotropic media: Izvestia, Earth Physics, **4**, 45–51.

Davydycheva, S., D. Homan, and G. Minerbo, 2009, Triaxial induction tool with electrode sleeve, FD modeling in 3D geometries: Journal of Applied Geophysics, **67**, 98–108.

Gianzero, S., D. Kennedy, L. Gao, and L. SanMartin, 2002, The response of a triaxial induction sonde in a biaxial anisotropic medium: Petrophysics, **43**, 172–184.

Kriegshäuser, B., O. Fanini, S. Forgang, G. Itskovich, M. Rabinovich, L. Tabarovsky, and M. Epov, 2000, A new multi-component induction logging tool to resolve anisotropic formation: 41st Annual Symposium, Society of Professional Well Log Analysts, Transactions, Paper D.

Kunz, K. S., and J. H. Moran, 1958, Some effects of formation anisotropy on resistivity measurements in boreholes: Geophysics, **23**, 770–794.

Lee, H. O., and F. L. Teixeira, 2007, Cylindrical FDTD analysis of LWD tools through anisotropic dipping-layered earth media: IEEE Transactions on Geoscience and Remote Sensing, **45**, no. 2, 383–388.

Lüling, M. G., R. Rosthal, and F. Shray, 1994, Processing and modeling 2-MHz tools in dipping, laminated, anisotropic formations: 35th Annual Symposium, Society of Professional Well Log Analysts, Transactions, Paper QQ.

Moran, J. H., and S. Gianzero, 1979, Effects of formation anisotropy on resistivity-logging measurements: Geophysics, **44**, 1266–1286.

———, 1982, Electrical anisotropy: Its effect on well logs, *in* A. A. Fitch, ed., Developments in geophysical exploration methods: Applied Science Publishers, 195–238.

Nekut, A. G., 1994, Anisotropy induction logging: Geophysics, **59**, 345–350.

Rabinovich, M., M. Gonfalini, T. Rocque, B. Corley, D. Georgi, L. Tabarovsky, and M. Epov, 2007, Multi-component induction logging: 10 years after: 48th Annual Symposium, Society of Professional Well Log Analysts, Transactions, Paper CC.

Rabinovich, M., L. Tabarovsky, B. Corley, J. van der Horst, and M. Epov, 2006, Processing multi-component induction data for formation dips and anisotropy: Petrophysics, **47**, 506–526.

Rosthal, R., T. Barber, S. Bonner, K.-C. Chen, S. Davydycheva, G. Hazen, D. Homan, C. Kibbe, G. Minerbo, R. Schlein, L. Villegas, H. Wang, and F. Zhou, 2003, Field test results of an experimental fully-triaxial induction tool: 44th Annual Symposium, Society of Professional Well Log Analysts, Transactions, Paper QQ.

Sawyer, W. K., C. I. Pierce, and R. B. Lowe, 1971, Electrical and hydraulic flow properties of Appalachian petroleum reservoir rocks: U. S. Bureau of Mines Report of Investigations 7519.

Wang, H., T. Barber, C. Morriss, R. Rosthal, R. Hayden, and M. Markley, 2006, Determining anisotropic formation resistivity at any relative dip using a multiarray triaxial induction tool: Annual Technical Conference and Exhibition, Society of Petroleum Engineers, SPE103113.

Wang, T. L., L. M. Yu, and O. Fanini, 2003, Multicomponent induction response in a borehole environment: Geophysics, **68**, 1510–1518.

Worthington, P. F., 1981, The influence of formation anisotropy upon resistivity-porosity relationship: 22nd Annual Symposium, Society of Professional Well Log Analysts, Transactions, Paper AA.

Zafran, Z. M., 1981, Studying the effect of sandstone anisotropy on quantitative interpretation of resistivity sounding and logging: 22nd Annual Symposium, Society of Professional Well Log Analysts, Transactions, Paper BB.

Zhang, J. H., and W. Y. Qiu, 2001, Residue theorem and application, *in* Functions of a complex variable, 3rd ed.: China Higher Education Press and Springer, 124–141.

Zhang, Z. Y., L. M. Yu, B. Kriegshäuser, and L. Tabarovsky, 2004, Determination of relative angles and anisotropic resistivity using multicomponent induction logging data: Geophysics, **69**, 898–908.

Zhao, J. L., X. Zhou, R. Chen, and C. Yang, 1994, Laboratory measurements and applications of anisotropy parameters of rocks: 35th Annual Symposium, Society of Professional Well Log Analysts, Transactions, Paper LL.
Zhdanov, M., D. Kennedy, and E. Peksen, 2001, Foundation of tensor induction well-logging: Petrophysics, **42**, 588–610.
Zhong, L. L., J. Li, L. C. Shen, and R. C. Liu, 2008, Computation of triaxial induction logging tools in layered anisotropic dipping formations: IEEE Transactions on Geoscience and Remote Sensing, **46**, no. 4, 1148–1163.